J. Fluid Mech. (2008), *vol.* 607, *pp.* 387–400.
doi:10.1017/S0022112008002103 Printed in the United Kingdom

Scaling laws for drag of a compliant body in an incompressible viscous flow

LUODING ZHU

Department of Mathematical Sciences, Indiana University–Purdue University Indianapolis, Indianapolis, IN 46202, USA
lzhu@math.iupui.edu

(Received 7 December 2007 and in revised form 23 April 2008)

Motivated by an important discovery on the drag scaling law (the 4/3 power law) of a flexible fibre in a flowing soap film by Alben *et al.* (*Nature* vol. 420, 2002, p. 479) at high Reynolds numbers ($2000 < Re < 40\,000$), we investigate drag scaling laws at moderate Re for a compliant fibre tethered at the midpoint and submerged in an incompressible viscous flow using the immersed boundary (IB) method. Our work shows that the scaling of drag with respect to oncoming flow speed varies with Re, and the exponents of the power laws decrease monotonically from approximately 2 towards 4/3 as Re increases from 10 to 800.

1. Introduction

The major energy expense in underwater transportation is in overcoming the resistance (drag) of the ambient fluid. One aim of a hydrodynamic design is to reduce the drag experienced by an immersed body (Steinberg 2002). Reduced drag means improved propulsion efficiency and lowered energy cost. Therefore drag reduction is an important topic. Much work has been done in this direction. For drag reduction of a rigid body in a flow, see the overview by Bushnell & Moore (1991) and references therein. For drag reduction of flexible aquatic animals in an aqueous environment, see Vogel (1996) and the survey by Fish (1998) and references therein. However, much less is known on how drag scales with the incoming flow speed for a compliant body moving in a viscous fluid.

Classic theory (Batchelor 1967) predicts that the drag of a rigid body in a rapidly flowing medium is proportional to the square of the oncoming medium speed. This law does not hold if the body is compliant, which may result in substantial drag reduction due to streamlining with the local flow. It was found that the power required to tow a flexing streamlined swimming body is significantly smaller than to tow a straight and rigid body at the same speed (Barrett *et al.* 1999). Recently Alben, Shelley & Zhang (2002, 2004), and Alben (2004) have investigated the drag reduction due to self-similar bending and streamlining of a flexible fibre in a two-dimensional flowing soap film, and discovered that the drag of the fibre scales as the 4/3 power of the incoming fluid speed at high Reynolds numbers. Schouveiler & Boudaoud (2006) investigated the rolling-up of a plastic thin neutrally buoyant sheet into a cone in a steady three-dimensional water flow. They found that the reconfiguration of the sheet led to a substantial decrease in the drag coefficient and obtained the drag coefficient as a function of the ratio of flow pressure and sheet flexure modulus. In all the above works the Reynolds numbers were very high.

Motivated by the work of Alben *et al.* (2002, 2004), Alben (2004), Zhu & Peskin (2007) studied the influence of flow and body parameters on the drag coefficient of an elastic fibre in a flowing viscous fluid at intermediate Re ($12.5 \leqslant Re \leqslant 375$). Zhu (2007) studied the vortex shedding of a flexible fibre in an incompressible viscous flow for Re between 30 and 800. Our current work studies scaling laws for the drag of a compliant fibre in a fast moving viscous fluid at moderate Reynolds numbers ($0.5 \leqslant Re \leqslant 800$), focusing on the influence of Reynolds number on the scaling of drag with respect to the oncoming flow speed using the immersed boundary (IB) method (Peskin 1977; Fauci & Peskin 1988; Tu & Peskin 1992; Fogelson 1992; Peskin & McQueen 1993; Peskin & Printz 1993; Fauci & Fogelson 1993; Peskin & McQueen 1996; Udaykumar, Shyy & Rao 1996; Roma, Peskin & Berger 1999; Ye *et al.* 1999; Cortez & Minion 2000; Lai & Peskin 2000; Peskin 2002; Zhu 2001, Mittal & Iaccarino, Griffith & Peskin 2005; Atzberger, Kramer & Peskin 2006; Kim & Peskin 2007; Taira & Colonius 2007; Mori & Peskin 2006).

We should point out that there are many other methods which are able to handle fluid–structure-interaction problems, such as the immersed interface method (LeVeque & Li 1994, 1997; Li & Lai 2001; Li 2006), the immersed finite element method (Zhang *et al.* 2004; Liu, Kim & Tang 2005), the extended immersed boundary method (Wang & Liu 2004), the immersed continuum method (Wang 2006, 2007), the level set method (Hou *et al.* 1997; Cottet & Maitre 2004; Xu *et al.* 2006; Cottet & Maitre 2006), the material point method (Sulsky, Chen & Schreyer 1994; Sulsky, Zhou & Schreyer 1995), the fictitious domain method (Glowinski, Pan & Periaux 1994*a*, *b*; Glowinski *et al.* 2001), and the Arbitrary Lagrangian Eulerian method (Hughes, Liu & Zimmerman 1981; Donea, Giuliani & Halleux 1982).

The remaining parts of the paper are as follows. In § 2 a model problem inspired by the laboratory experiment in Alben *et al.* is described. The immersed boundary (IB) formulation of the model problem and the related numerical discretization are given in § 3. Section 4 addresses the drag scaling laws. We conclude with a summary and discussion in § 5.

2. Model problem

To mimic the laboratory experiment reported in Alben *et al.* we consider an incompressible viscous fluid flowing in a two-dimensional vertical tunnel driven by gravity and falling against air resistance. An elastic fibre is initially placed horizontally at the tunnel centre with the midpoint fixed near the top boundary. See figure 1. The tunnel's two sidewalls are rigid and a no-slip boundary condition is used for the velocity on the sidewalls. The top and bottom boundaries are open and the velocity is specified at the inlet and outlet. The characteristic quantities in our problem are: fluid density ρ_0, fluid viscosity ν, inflow speed V_0, fibre length L, fibre flexure modulus K_b, fibre stretching modulus K_s, fibre linear mass density M, and the flow tunnel width W. By dimensional analysis, there exist six independent dimensionless parameters in our problem: Reynolds number Re, dimensionless fibre flexure modulus $\hat{K}_b$, dimensionless fibre mass density $\hat{M}$, dimensionless fibre length $\hat{L}$, Froude number Fr, and dimensionless fibre stretching coefficient $\hat{K}_s$. See § 4 for definitions of these dimensionless parameters and their values used in our work.

Since Zhu & Peskin (2007) showed that the drag coefficient is not sensitive to $\hat{M}$ in a range that contains the value of $\hat{M}$ in the laboratory experiment (Alben *et al.* 2002), and in our simulations the fibre is made almost inextensible by using sufficiently large values of $\hat{K}_s$, we assume that the effects of $\hat{M}$ and $\hat{K}_s$ on drag and drag coefficient

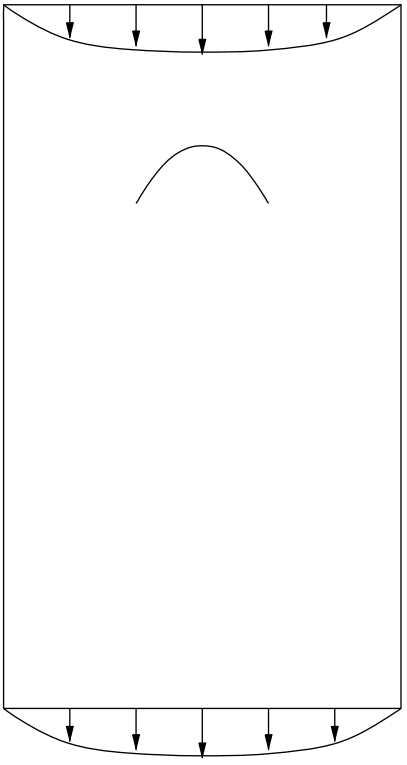

FIGURE 1. A diagram of the model problem abstracted from the laboratory experiment. The rectangle represents the flow tunnel. The curve in the centre represents a deformed fibre. The arrows indicate the flow direction. The curves under the arrows represent the magnitude of the inflow speed (not to scale). See figure 2 for the exact inflow/outflow velocity profile.

are negligible. Consequently the fibre is treated as neutrally buoyant in the fluid for our problem. Previous work (Zhu 2007) has found that the drag coefficient (C_d) varies with dimensionless fibre length $\hat{L}$: C_d increases with $\hat{L}$ in the range (0.17, 0.6). To minimize this effect, the value of $\hat{L}$ is kept in a small interval (0.2, 0.3) over which drag coefficient changes only slightly. (The channel width W is kept fixed in all simulations. The variation in $\hat{L}$ is caused by different fibre lengths.) Hence the influence of $\hat{L}$ is not considered explicitly here. Furthermore, the influence of Fr is thought to be insignificant for the range used in our work ($21 \leqslant Fr \leqslant 40$). Therefore in this paper we explore only the effects of Reynolds number and dimensionless flexure modulus on drag and drag coefficient, focusing on the scaling laws of drag with respect to the oncoming flow speed for various Reynolds numbers.

3. The immersed boundary formulation of the model problem

3.1. *The governing equations*

The fluid mass density ρ_0, the channel width W, and the inflow speed V_0 are chosen as the characteristic quantities for non-dimensionalization of the problem. The governing equations in dimensionless form for the model problem are as follows. The two-dimensional incompressible viscous Navier–Stokes equations are used to describe the

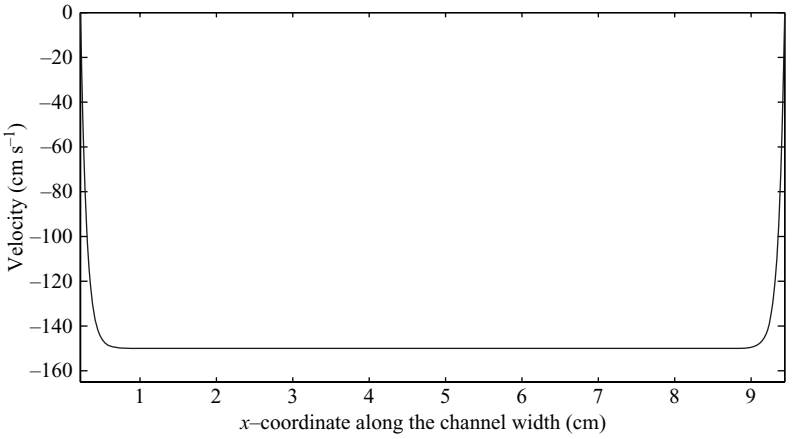

FIGURE 2. A typical inflow velocity profile for inflow speed 150 cm s^{-1}. The x-axis is the tunnel width. The y-axis is the vertical velocity component $V(x)$.

motion of both the fluid, which is a soap film, and the fibre (the Einstein summation convention is used in this Section for $i = 1, 2$ and $j = 1, 2$):

$$\frac{\partial u_i}{\partial t} + u_j \frac{\partial u_i}{\partial x_j} = -\frac{\partial p}{\partial x_i} + \frac{1}{Re}\frac{\partial}{\partial x_j}\left(\frac{\partial u_i}{\partial x_j}\right) + f_i - \frac{1}{Fr}u_i - g_i, \tag{3.1}$$

$$\frac{\partial u_i}{\partial x_i} = 0. \tag{3.2}$$

The vector $(g_1, g_2) = (0, 1/Fr)$. The term $(-1/Fr)u_i$ models the air resistance where the resistance coefficient is $1/Fr$. The resistance to the flowing soap film due to the ambient air is assumed to be proportional to the flowing film velocity. This assumption is justified by the fact that the stationary velocity profile $V(x)$ of the soap film falling subject to gravity and air resistance without the fibre is found to be constant over the majority of the tunnel width, which agrees very well with the experimental measurements (Alben *et al.* 2002). See figure 2 for such a profile of $V(x)$. The vector $(f_1, f_2) = \boldsymbol{f}(\boldsymbol{x}, t)$ is the Eulerian force density defined on a fixed Eulerian mesh, which is calculated from the Lagrangian force density $\boldsymbol{F}(s, t) = (F_1, F_2)$ defined on the Lagrangian mesh by

$$f_i = \int F_i(\alpha, t)\delta(x_1 - X_1(\alpha, t))\delta(x_2 - X_2(\alpha, t))\,\mathrm{d}\alpha \tag{3.3}$$

where $\delta(x_i)$ is the Dirac delta function associated with the x_i-direction; α is the Lagrangian coordinate associated with the fibre; t is the time variable. The vector $(X_1, X_2) = \boldsymbol{X}(\alpha, t)$ is the fibre configuration, i.e. the Eulerian coordinate of a fibre point with Lagrangian coordinate α. The Lagrangian force density $\boldsymbol{F}(\alpha, t) = (F_1, F_2)$ is defined as

$$F_i(\alpha, t) = -\frac{1}{L}\frac{\partial \mathscr{E}}{\partial X_i}. \tag{3.4}$$

The total elastic potential energy density $\mathscr{E} = \mathscr{E}_s + \mathscr{E}_b$, where the energy generated by stretching ($\mathscr{E}_s$) and bending ($\mathscr{E}_b$) are computed respectively, by

$$\mathscr{E}_s = \frac{1}{2}\hat{K}_s \int \left(\sqrt{\frac{\partial X_i}{\partial \alpha}\frac{\partial X_i}{\partial \alpha}} - 1 \right)^2 \mathrm{d}\alpha, \tag{3.5}$$

$$\mathscr{E}_b = \frac{1}{2}\hat{K}_b \int \frac{\partial^2 X_i}{\partial \alpha^2}\frac{\partial^2 X_i}{\partial \alpha^2}\,\mathrm{d}\alpha. \tag{3.6}$$

The constant $\hat{K}_s$ is the fibre stretching coefficient which is chosen in the computations so that the fibre is almost inextensible, and the constant $\hat{K}_b$ is the dimensionless flexure modulus.

The motion of the fibre is described by

$$\frac{\partial X_i}{\partial t}(\alpha, t) = \int u_i \delta(x_1 - X_1(\alpha, t))\delta(x_2 - X_2(\alpha, t))\,\mathrm{d}x_1\,\mathrm{d}x_2. \tag{3.7}$$

The initial condition for the velocity is the steady velocity field $(0, V(x))$ of the flow problem in the absence of the fibre. Note that $V(x)$ is not a parabola because of the presence of air resistance. See figure 2. It is constant in the majority of the tunnel width. The maximum value of $V(x)$ is used as the inflow speed V_0. The pressure is zero everywhere at the initial instant (i.e. a solution to the Laplace equation under periodic boundary conditions). The no-slip condition is applied on the two rigid sidewalls for velocity. The initial velocity profile is imposed on the inlet and outlet. Periodic boundary conditions are used for pressure. This is because in the immersed boundary method the physical domain (the two-dimensional rectangular channel in our problem) is imbedded in a slightly larger two-dimensional rectangular computational domain, and periodic boundary conditions are used for the flow variables along each direction for this artificial computational domain. The initial configuration of the fibre is a horizontal line segment situated at the channel centre with the midpoint ($\boldsymbol{X}_f$) fixed. The coordinate for the fixed point is (0.5, 1.8). No other part of the fibre is constrained. The boundary condition for the fibre is $\boldsymbol{X}_f = (0.5, 1.8)$. The initial fibre velocity is zero with respect to the fluid.

3.2. *Discretization*

The above nonlinear system of differential-integral equations (3.1)–(3.7) is discretized on a fixed Eulerian coordinate by a finite difference method. The nonlinear terms in the Navier–Stokes equations are linearized by using the velocity at the previous time-step. The skew-symmetrical scheme is used for the convection terms. The centred difference scheme is used for the spatial derivatives. The backward Euler is used for the time derivatives. The resultant linear system of algebraic equations with constant coefficients is solved numerically by discrete fast Fourier transforms. See Peskin (1977), Peskin & McQueen (1993, 1996), Peskin (2002) and Zhu (2001) for details of this approach.

The computations are performed on a fixed Eulerian mesh 256×512 for the fluid on a 1×2 rectangular domain (dimensionless). The resolution for fibre discretization is nearly half of that for the fluid. The time-step size is 1.3×10^{-4}. For details of the convergence of drag with respect to spatial meshes and time-step size, see Zhu & Peskin (2007).

Name	Definition	Range
Reynolds number (Re)	$\frac{V_0 L}{\nu}$	0.5–800
Dimensionless flexure modulus ($\hat{K}_b$)	$\frac{K_b}{\rho_0 V_0^2 L^3}$	4.1×10^{-7}–5×10^3
Dimensionless mass density ($\hat{M}$)	$\frac{M}{\rho_0 L}$	1
Dimensionless stretching coeff. ($\hat{K}_s$)	$\frac{K_s}{\rho_0 V_0^2 L}$	1.2×10^6–1.0×10^7
Dimensionless fibre length ($\hat{L}$)	$\frac{L}{W}$	0.2–0.3
Froude number (Fr)	$\frac{V_0^2}{gL}$	21–40

TABLE 1. Dimensionless parameters used in the simulations. See § 2 for the meanings of the symbols in defining the dimensionless parameters.

4. Main results

The instantaneous drag of the fibre is computed as the y-component of the tension vector at the tethered point $\boldsymbol{X}_f$. A time-averaged drag $\bar{D}$ is calculated as an average of the instantaneous drag over 200 equally spaced instants after the initial transition dies out. See Zhu & Peskin (2007) for details. A time-averaged drag coefficient $\bar{C}_d$ is defined as

$$\bar{C}_d = \frac{\bar{D}}{\frac{1}{2}\rho_0 {V_0}^2 L}.$$

(Frontal area is used as reference area in defining $\bar{C}_d$.) Following the work of Alben *et al.*, an additional dimensionless quantity

$$\eta = \sqrt{\frac{\rho_0 V_0^2 L^3/2}{K_b}}$$

and a dimensionless drag $D = \bar{C}_d \eta^2$ are introduced. The parameter η measures the relative importance of fluid kinetic energy and fibre elastic potential energy. It is connected to the dimensionless flexure modulus $\hat{K}_b$ by $\eta = (2\hat{K}_b)^{-1/2}$. Note that (i) a greater η (or a smaller $\hat{K}_b$) indicates a more compliant fibre; (ii) as D scales with η the drag scales with the inflow speed V_0 (Alben *et al.* 2002). The values of all the important dimensionless parameters used in this work are listed in table 1.

The main computational results are given as follows: first some typical deformed fibre shapes are given; then the influence of Re on $\bar{C}_d$ for different values of $\hat{K}_b$ is reported; then scaling laws for the dimensionless drag D with respect to η for different Re are discussed.

It is illustrative to show some typical fibre shapes in the flowing soap film. Figure 3 plots some deformed fibre shapes (time-averaged) for $Re = 192$. The fibre length was 3.5 cm; the inflow speed was 220 cm s^{-1}; the dimensionless flexure modules η ranged from 0.01 (corresponding to the outermost straight line) to 1100 (corresponding to the innermost curve). Note that a few fibre shapes overlap the horizontal line, and the shapes of the two innermost fibres are very close. The left and right branches for these two fibre shapes are not exactly symmetrical, which might be caused by numerical errors when η is too large (see § 5). It is worth pointing out that the two

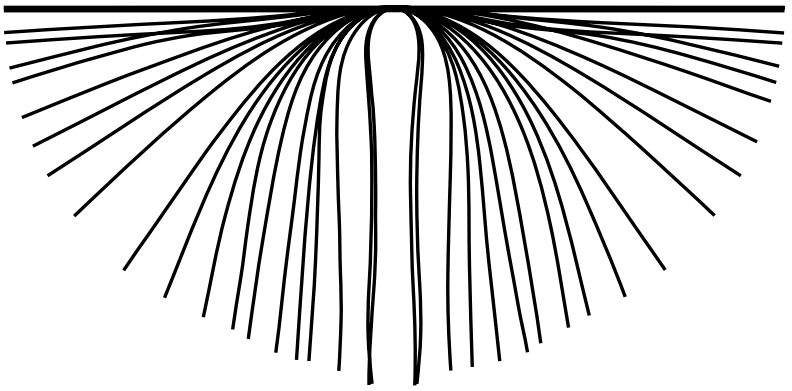

FIGURE 3. Some typical time-averaged deformed fibre shapes. The fibre length was 3.5 cm; the inflow speed was $220\,\mathrm{cm\,s^{-1}}$; $Re = 192$; $\eta = [0.01, 1100]$. The outermost straight line corresponds to $\eta = 0.01$; the innermost shape corresponds to $\eta = 1100$. Note that a few fibre shapes overlap the horizontal line, and the shapes of the two innermost fibres are very close.

sidewalls may have a strong effect on the shape of the fibre at high Re: the walls may force the fibre to be more streamlined and more aligned with the local flow than in the unbounded case (in the absence of the sidewalls). See Wu, Whitney & Lin (1969) and Wu (1972) for the wall effect on cavity and wake flows. See Zhu & Peskin (2007) and Zhu (2007) for more fibre shapes and the influence of flow and fibre parameters, including the wall effect, on the fibre shapes.

Figure 4(a) plots the averaged drag-coefficient $\bar{C}_d$ versus Reynolds number Re for three different values of the dimensionless flexure modulus $\hat{K}_b$: $\hat{K}_b = 1.299 \times 10^{-1}$; $\hat{K}_b = 1.299 \times 10^{-2}$; $\hat{K}_b = 1.299 \times 10^{-3}$. As expected, the datum of $\bar{C}_d$ associated with the smallest $\hat{K}_b$ is lowest, the datum associated with the greatest $\hat{K}_b$ is highest, and the datum associated with the intermediate $\hat{K}_b$ sits between for each value of Re considered here. This implies that the decrease of $\hat{K}_b$, i.e. the increase of body flexibility, is responsible for the reduction of $\bar{C}_d$. Note that in each case, when Re is sufficiently high, e.g. $Re > 200$, the averaged drag-coefficient is nearly constant. The reason is as follows: to single out the sole influence of Re on $\bar{C}_d$, all the dimensional parameters (including K_b) must be fixed except the kinematic viscosity ν which varies with Re. When Re is sufficiently high the total drag is dominated by the form drag which depends on the deformed fibre shape. The fibre shape changes only slightly with Re in the range of [200, 800] (see Zhu 2007), therefore the total drag remains nearly constant, and also the drag coefficient $\bar{C}_d$. But when Re is smaller, $\bar{C}_d$ increases as Re decreases. $\bar{C}_d$ increases slowly at first, and then rapidly when $Re < 100$. The swift increase of $\bar{C}_d$ results from the swift increase of skin friction which dominates the drag as Re becomes small enough.

Figure 4(b) plots the same data by the same symbols on a log-log scale. The solid line represents the function $\bar{C}_d = 10/Re$. We can see that the drag-coefficient scales with $1/Re$ when Re is sufficiently small (e.g. $Re \leqslant 5$), irrespective of the value of $\hat{K}_b$. This seems to indicate that body flexibility and streamlining is not very beneficial for drag reduction when drag is dominated by skin friction. Notice that the prefactor of $1/Re$ is strongly dependent on $\hat{K}_b$. Our simulation results suggest that a smaller value of $\hat{K}_b$ has a lower prefactor. For $5 \leqslant Re \leqslant 200$, both skin friction and form drag appear to be equally significant.

The log-log plot shows that the power at which $\bar{C}_d$ grows with Re is not a constant in general. It varies with Re between around 0 when Re is large and around -1 when

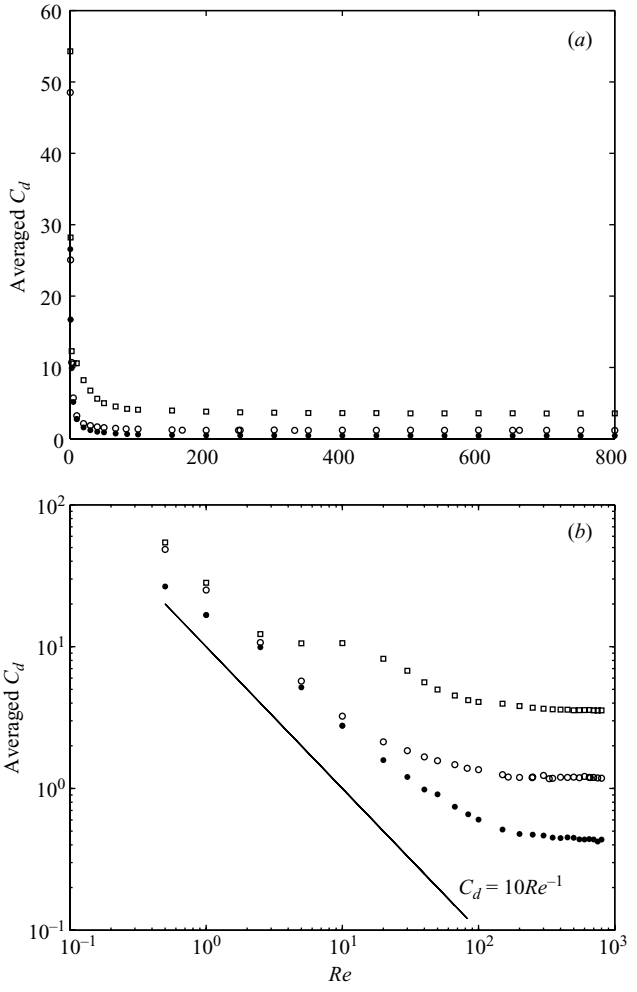

FIGURE 4. The averaged drag-coefficient $\bar{C}_d$ versus Reynolds number Re for three different values of dimensionless flexure modules $\hat{K}_b$: (*a*) a regular plot; (*b*) a log-log plot. □, $\hat{K}_b = 1.299 \times 10^{-1}$ ($\eta = 1.96$); ○, $\hat{K}_b = 1.299 \times 10^{-2}$ ($\eta = 6.20$); ●, $\hat{K}_b = 1.299 \times 10^{-3}$ ($\eta = 19.6$). The solid line on (*b*) is the function $\bar{C}_d = (10/Re)$.

Re is small. The differing behaviour of the data shown by squares, and that shown by open and filled circles, at $5 \leqslant Re \leqslant 100$ may be explained by the significantly larger value of $\hat{K}_b$ (10 to 100 times greater than the two others) in the 'squares' case, where the fibre is close to being rigid. Note that the C_d versus Re curves bear some similarity to the classic $C_d - Re$ curve for a rigid circular cylinder (Batchelor 1967): scaling as Re^{-1} for low Re and nearly a constant for higher Re, and the transition part between low and high Re is roughly concave up (except for the case with $\hat{K}_b = 0.13$ where the transition curve possesses an inflection point). It should be pointed out that the transition to the Re^0 scale (i.e. C_d is roughly constant) occurs at much smaller Re in our case (400–500) than the cylinder case (nearly 10^3). Presumably this is caused by the additional physics (body flexibility) in our case.

Figure 5 plots on a log-log scale the dimensionless drag D versus the dimensionless η for six different Reynolds numbers: $Re = 10$; $Re = 55$; $Re = 123$; $Re = 192$; $Re = 500$; $Re = 800$. The dotted and dashed lines are functions $D = \eta^2$ and $D = \eta^{4/3}$,

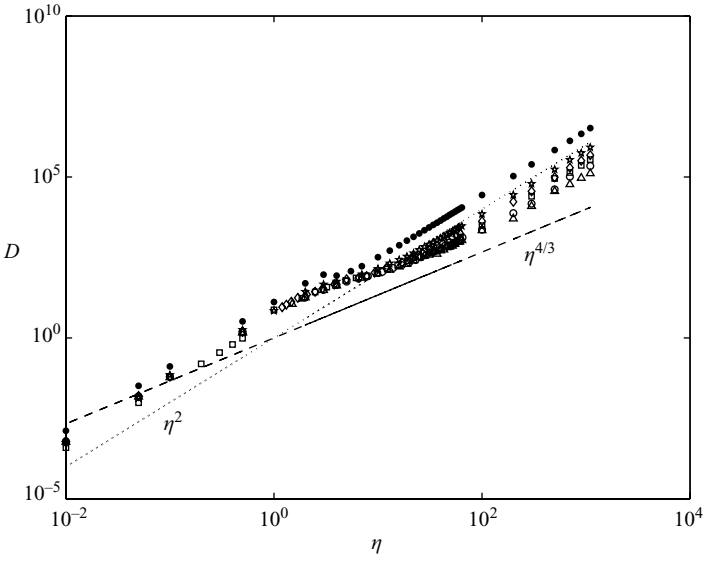

FIGURE 5. The dimensionless drag D versus η for six values of Re on a log-log scale. ●, $Re = 10$; ∗, $Re = 55$; ◇, $Re = 123$; □, $Re = 192$; ○, $Re = 500$; Δ for $Re = 800$. The dotted line is the function $D = \eta^2$, the dashed line is $D = \eta^{4/3}$.

respectively. We see from the figure 5 that the data corresponding to different Re do not collapse to a single curve on the log-log plot, and the data corresponding to a fixed Re do not entirely lie on a straight line either. This indicates that the dimensionless drag D does not scale as a single power of η in general at lower Reynolds numbers. It appears that there exists a transition interval of η above/below which the data for a fixed Re are nearly situated on a line. For the range of Re considered in this paper, the interval is approximately (1, 10). We can see from figure 5 that when $\eta > 10$, D scales almost as η^2 for $Re = 10$ (the data shown by filled circles almost parallel to $D = \eta^2$). But when $Re = 800$, the associated data clearly deviate from the line of η^2 on a log-log scale.

To quantify the powers in the drag scaling, the method of least squares is used to fit the data of D for $\eta \geqslant 10$ for each value of Re. See figure 6 for details. The six plots correspond to six values of Re. In each plot the x-axis is the dimensionless η, the y-axis is the dimensionless drag D. The filled circles represent the drag data, and the solid line is the linear function fitting the data best in the least squares sense. For comparison, the functions $D = \eta^2$ (dotted line) and $D = \eta^{4/3}$ (dashed line) are plotted as well. The results are as follows: the power is 1.97, 1.89, 1.83, 1.77, 1.63, 1.56 for $Re = 10, 55, 123, 192, 500, 800$, respectively. (Note that there is a fair amount of uncertainty in the scaling exponents because of the limited amount of drag data used.) Notice that the power starts at nearly 2 and decreases monotonically towards 4/3 as Re increases from 10 to 800. This shows that the scaling law of the drag of a compliant body moving in an incompressible viscous fluid depends on Reynolds number, which may be explained by the fact that the drag is dominated by form drag (related to fluid inertial forces) when Re is high and by skin friction (related to fluid viscous forces) when Re is low. When Re is sufficient small, the viscous friction forces dominate the drag, and drag reduction due to streamlining and alignment with the flow is not significant. As a consequence, the total fibre drag and therefore the drag coefficient $\bar{C}_d$ are nearly constant. Perhaps this is the reason why D scales

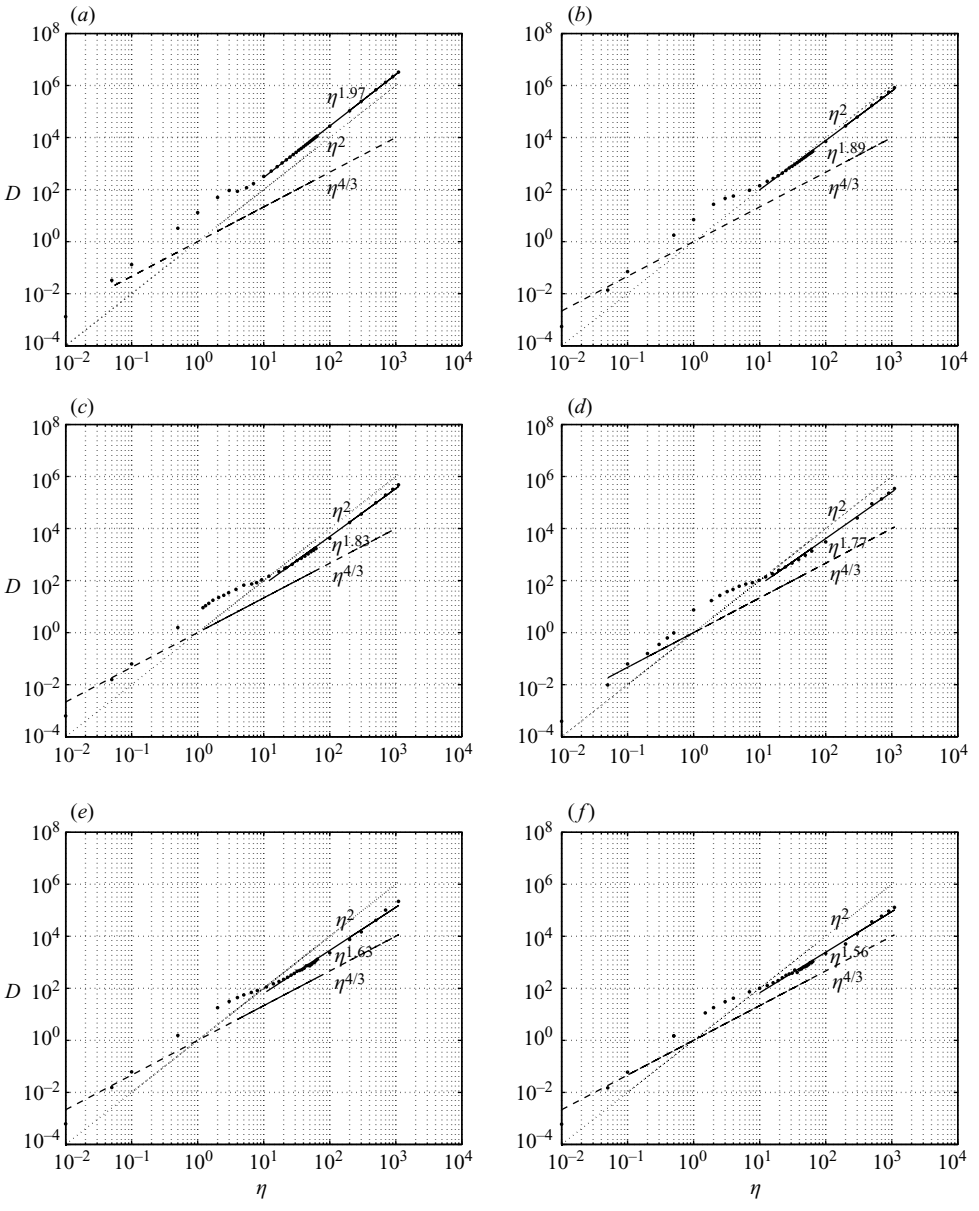

FIGURE 6. The dimensionless drag D versus η on a log-log plot for six Reynolds numbers: (*a*) $Re = 10$, (*b*) $Re = 55$, (*c*) $Re = 123$ (*d*), $Re = 192$, (*e*) $Re = 500$, (*f*) $Re = 800$. In each plot the filled circles are drag data, the solid line is the linear function fitting the data best in the least squares sense for $\eta \geqslant 10$ on a log-log scale. Three power functions are labelled on each figure: η^2 (dotted line), $\eta^{4/3}$ (the dashed line), and η^n (solid line) representing the drag growth where the power n is the slope of the fitting line, which varies from 1.97 to 1.56.

approximately as the square of η at $Re = 10$. Again, the η^2-growth of drag for $Re = 10$ seems to indicate that body flexibility is not very effective in reducing drag at a small Re. This is consistent with the fact that tiny swimming organisms do not appear streamlined (Vogel 1996).

Another relevant important piece of fundamental work on body flexibility in low-Re flows is Wiggins & Goldstein (1998) where a critical bending modulus was found at which a flagellum (which could be idealized in two dimensions as a fibre) generates maximum propulsive force when driven sinusoidally at the leading edge. For more information on hydrodynamic forces and body flexibility with applications to organisms living in rapidly moving fluids, refer to Vogel (1984, 1989), Koehl (1984), Koehl, Hunter & Jed (1991), and Denney (1994).

For very high Re flows, Albert *et al.* (2002) has identified a critical value of η around $O(1)$, below which the drag grows as the second power, akin to the case of a rigid body. The similar η_c in our work is around 1–10. It is seen from figure 6 that below the transition interval (1, 10), the drag D approximately scales as η^2 for all the values of Re reported here. This is because when η is small enough the fibre becomes a rigid plate placed almost perpendicular to the oncoming flow. Therefore the drag is approximately proportional to the square of the incoming flow speed.

In the transition regime the scaling exponent is not even approximately a constant; it varies with η for each of the Reynolds number considered here. The D versus η curves look similar to one another: they are all convex in (1,10). Notice that the transition exists for all Re considered in our work, and it does not vanish when Re is taken to infinity (Alben *et al.* 2002). It appears that within this regime the bending of the fibre is not self-similar (the fibre shapes are not self-similar), therefore the drag does not scale as a constant power.

5. Summary and discussion

Using the IB method, we computed the drag of a compliant fibre fixed at the midpoint and immersed in a flowing viscous incompressible fluid for $\hat{K}_b$ in the range $[4.1 \times 10^{-7}, 5 \times 10^3]$ and Re in the range [0.5, 800]. The least squares method is used to fit the data from a fixed Reynolds number to a linear function for $\eta \geqslant 10$, and various power laws are found corresponding to different Reynolds numbers. In particular, we have found that for $\eta \geqslant 10$, the drag D scales as nearly η^2 for $Re = 10$, and the power monotonically decreases from nearly 2 towards 4/3 as Re increases from 10 to 800. Our simulation results show that drag reduction due to body flexibility occurs at intermediate Re as well, but not very efficient at low Re.

An immediate question arises: would the growth power attain 4/3 as Re becomes higher, e.g. in the interval (800, 2000)? (The Reynolds numbers in Alben *et al.*'s work were between 2000 and 40 000.) It would be interesting to extend our current work to $800 < Re < 2000$ to address this. Currently, however, we are not able to do this because of difficulty in solving a viscous flow with higher Re by the particular IB method we use.

For an infinitely flexible fibre, i.e. the flexure modulus approaches zero or η approaches infinity, the fibre is expected to be folded in half and aligned with the flow. In this case, the skin friction dominates and the drag should scale as $\eta^{3/2}$ (Batchelor 1967). However our numerical simulations could not replicate this scaling because of the numerical instability caused by the extremely small values of the flexure modulus: the fibre always tends to become unstable (oscillate or flap).

Drag mainly consists of form drag (dominating when Re is sufficiently large) and skin friction (dominating when Re is sufficiently small). It would be interesting to decompose the total drag into the two components. Unfortunately we have not yet

successfully obtained such a decomposition because of practical numerical difficulties. This work is continuing.

There are six dimensionless quantities in our problem: Re, $\hat{K}_b$ (or η), $\hat{M}$, $\hat{L}$, Fr, $\hat{K}_s$. In principle, the drag D and drag-coefficient $\bar{C}_d$ are functions of these six dimensionless parameters. We have considered two of them under the assumption that the remaining ones do not have significant effects. It would be a nice piece of future work to show how these parameters might modify the drag scaling laws for values outside the ranges used in this paper. Because of computational limitations, we have to postpone this task.

In the laboratory experiment the soap film was approximately 1–3 μm in thickness, and the fibre diameter was approximately 34 μm. In our model problem, both the soap film and the fibre are considered as non-Brownian. It would be interesting to model the fluid or the fibre or both as Brownian and find how the drag scaling laws would be modified accordingly. This is another piece of future work.

The author would like to thank the referees for their suggestions and comments. The author also thanks the USA National Science Foundation for the partial support of the work under research grant DMS-0713718.

REFERENCES

Alben, S. 2004 Drag reduction by self-similar bending and a transition to forward flight by a symmetry breaking instability. PhD thesis, Courant Institute of Mathematical Sciences, New York University.

Alben, S., Shelley, S. & Zhang, J. 2002 Drag reduction through self-similar bending of a flexible body. *Nature* **420**, 479–481.

Alben, S., Shelley, S. & Zhang, J. 2004 How flexibility induces streamlining in two-dimensional flow. *Phys. Fluids* **16**, 1694–1713.

Atzberger, P. J., Kramer, P. R. & Peskin, C. S. 2006 A stochastic immersed boundary method for biological fluid dynamics at microscopic length scale. *J. Comput. Phys.* **224**, 1255–1292.

Barrett, D. S., Triantafyllou, M. S., Yue, D. K. P., Grosenbaugh, M. A. & Wolfgang, M. J. 1999 Drag reduction in fish-like locomotion. *J. Fluid Mech.* **392**, 183–212.

Batchelor, G. K. 1967 *An Introduction to Fluid Dynamics.* Cambridge University Press.

Bushnell, D. M. & Moore, K. J. 1991 Drag reduction in Nature. *Annu. Rev. Fluid Mech.* **23**, 65–79.

Cortez, R. & Minion, M. 2000 The blob projection method for immersed boundary problems. *J. Comput. Phys.* **161**, 428–453.

Cottet, G. H. & Maitre, E. 2004 A level set formulation of immersed boundary methods for fluid-structure interaction problems. *C.R. Acad. Sci. Paris* I **338**, 581–586.

Cottet, G. H. & Maitre, E. 2006 A level set method for fluid-structure interactions with immersed interfaces. *Math. Models Meth. Appl. Sci.* **16**, 415–438.

Denny, M. W. 1994 Extreme drag forces and the survival of wind and water-swept organisms. *J. Expl Biol.* **195**, 97–115.

Donea, J., Giuliani S. & Halleux, J. P. 1982 An Arbitrary Lagrangian- Eulerian finite element method for transient dynamic fluid structure interactions. *Comput. Meth. Appl. Mech. Engng* **33**, 689–723.

Fauci, L. J. & Fogelson, A. L. 1993 Truncated Newton methods and the modeling of complex elastic structures. *Commun. Pure Appl. Maths* **46**, 787–818.

Fauci, L. J. & Peskin, C. S. 1988 A computational model of aquatic animal locomotion. *J.Comput. Phys.* **77**, 85–108.

Fish, F. E. 1998 Imaginative solutions by marine organisms for drag reduction. In *Proc. Intl Symp. on Seawater Drag Reduction, Newport, Rhode Island* (ed. J. C. S. Meng), pp. 443–450.

Fogelson, A. L. 1992 Continuum models of platelet aggregation: Formulation and mechanical properties. *SIAM J. Appl. Maths* **52**, 1089–1110.

Glowinski, R., Pan, T., Hesla, T., Joseph, D. & Periaux, J. 2001 A fictitious domain approach to the direct numerical simulation of incompressible viscous flow past moving rigid bodies: Application to particulate flow. *J. Comput. Phys.* **169**, 363–426.

Glowinski, R., Pan, T. & Periaux, J. 1994*a* A fictitious domain method for Dirichlet problem and applications. *Comput. Meth. Appl. Mech. Engng* **111**, 283–303.

Glowinski, R., Pan, T. & Periaux, J. 1994*b* A fictitious domain method for external incompressible viscous flow modeled by Navier-Stokes equations. *Comput. Meth. Appl. Mech. Engng* **112**, 133–148.

Griffith, B. E. & Peskin, C. S. 2005 On the order of accuracy of the immersed boundary method: Higher order convergence rates for sufficient smooth problems. *J. Comput. Phys.* **208**, 75–105.

Hughes, T. J. R., Liu, W. & Zimmerman, T. K. 1981 Lagrangian-Eulerian finite element formulation for incompressible viscous flows. *Comput. Meth. Appl. Mech. Engng* **29**, 329–349.

Hou, T. Y., Li, Z. L., Osher, S., Zhao, H. K. 1997 A hybrid method for moving interface problems with application to the Hele-Shaw flow. *J. Comput. Phys.* **134**, 236–252.

Kim, Y. & Peskin, C. S. 2007 Penalty immersed boundary method for an elastic boundary with mass. *Phys. Fluids* **19**, 053103.

Koehl, M. A. R. 1984 How do benthic organisms withstand moving water?. *Am. Zool.* **24**, 57–70.

Koehl, M. A. R., Hunter, T. & Jed, J. 1991 How do body flexibility and length affect hydrodynamic-forces on sessile organisms in waves versus in currents. *Am. Zool.* **31**, A60–A60.

Lai, M. C. & Peskin, C. S. 2000 An immersed boundary method with formal second order accuracy and reduced numerical viscosity. *J. Comput. Phys.* **160**, 705–719.

LeVeque, R. J. & Li, Z. L. 1994 The immersed interface method for elliptic equations with discontinuous coefficients and singular sources. *SIAM J. Numer. Anal.* **31**, 1019–1044.

LeVeque, R. J. & Li, Z. L. 1997 Immersed interface methods for Stokes flows with elastic boundaries or surface tension. *SIAM J. Sci. Comput.* **18**, 709–735.

Li, Z. L. 2006 *The Immersed Interface Method – Numerical Solutions of PDEs Involving Interfaces and Irregular Domains*. SIAM, Philadelphia.

Li, Z. L. & Lai, M. C. 2001 Immersed interface methods for Navier-Stokes equations with singular forces. *J. Comput. Phys.* **171**, 822–842.

Liu, W. K., Kim, D. K. & Tang, S. 2007 Mathematical foundations of the immersed finite element method. *Comput. Mech.* **39**, 211–222.

Mittal, R. & Iaccarino, G. 2005 Immersed boundary methods. *Annu. Rev. Fluid Mech.* **37**, 239–261.

Mori, Y. & Peskin, C. S. 2006 Implicit second-order immersed boundary method with boundary mass. *J. Comput. Phys.* (submitted).

Peskin, C. S. 1977 Flow patterns around heart valves: a numerical method. *J. Comput. Phys.* **25**, 220–252.

Peskin, C. S. 2002 The immersed boundary method. *Acta Numerica* **11**, 479–517.

Peskin, C. S. & McQueen, D. M. 1993 Computational biofluid dynamics. *Contemp. Maths* **141**, 161–186.

Peskin, C. S. & McQueen, D. M. 1996 Fluid dynamics of the heart and its valves. In *Case Studies in Mathematical Modeling: Ecology, Physiology, and Cell Biology* (ed. H. G. Othmer, F. R. Adler, M. A. Lewis & J. C. Dallon), P. 309. Prentice-Hall.

Peskin, C. S. & Printz, B. F. 1993 Improved volume conservation in the computation of flows with immersed elastic boundaries. *J. Comput. Phys.* **105**, 33–46.

Roma, A. M., Peskin, C. S. & Berger, M. J. 1999 An adaptive version of the immersed boundary method. *J. Comput. Phys.* **153**, 509–534.

Schouveiler, L. & Boudaoud, A. 2006 The rolling up of sheets in a steady flow. *J. Fluid Mech.* **563**, 71–80.

Steinburg, V. 2002 Bend and survive. *Nature* **420**, 473–473.

Sulsky, D., Chen, Z. & Schreyer, H. L. 1994 A particle method for history-dependent materials. *Comput. Mech. Appl. Mech. Engng* **118**, 179–197.

Sulsky, D., Zhou, S. J. & Schreyer, H. L. 1995 Application of a particle-in-cell method to solid mechanics. *Comput. Phys. Commun.* **87**, 136–152.

Taira, K. & Colonius, T. 2007 The immersed boundary method: a projection approach. *J. Comput. Phys.* **225**, 2118–2137.

Tu, C. & Peskin, C. S. 1992 Stability and instability in the computation of flows with moving immersed boundaries: A comparison of three methods. *SIAM J. Sci. Statist. Comput.* **13**, 1361–1376.

Udaykumar, H. S., Shyy, W., Rao, M. M. 1996 A mixed Eulerian-Lagrangian method for fluid flows with complex and moving boundaries. *Intl J. Numer. Meth. Fluids* **22**, 691–712.

Vogel, S. 1984 Drag and flexibility in sessile organisms. *Am. Zool.* **24**, 37–44.

Vogel, S. 1989 Drag and reconfiguration of broad leaves in high winds. *J. Expl Bot.* **40**, 941–948.

Vogel, S. 1996 *Life in Moving Fluids – The Physical Biology of Flow*. Princeton University Press.

Wang, X. 2006 From immersed boundary method to immersed continuum method. *Intl J. Multiscale Comput. Engng* **4**, 127–145.

Wang, X. 2007 An iterative matrix-free method in implicit immersed boundary/continuum methods. *Computers Struct.* **85**, 739–748.

Wang, X. & Liu, W. K. 2004 Extended immersed boundary method using FEM and RKPM. *Comput. Meth. Appl. Mech. Engng* **193**, 1305–1321.

Wiggins, C. H. & Goldstein, R. E. 1998 Flexive and propulsive dynamics of elastica at low Reynolds number. *Phys. Rev. Lett.* **80**, 3879–3882.

Wu, T. Y. 1972 Cavity and wake flows. *Annu. Rev. Fluid Mech.* **4**, 243–284.

Wu, T. Y., Whitney, A. K. & Lin, J. D. 1969 Wall effect in cavity flows. *Calif. Inst. Technol. Rep.* E-111A.5

Xu, J., Li, Z., Lowengrub, J. & Zhao, H. 2006 A level set method for interfacial flows with surfactant. *J. Comput. Phys.* **212**, 590–616.

Ye, T., Mittal, R., Udaykumar, H. S. & Shyy, W. 1999 An accurate Cartesian grid method for viscous incompressible flows with complex immersed boundaries. *J. Comput. Phys.* **156**, 209–240.

Zhang, L., Gersternberger, A., Wang, X. & Liu, W. K. 2004 Immersed finite element method. *Comput. Meth. Appl. Mech. Engng* **193**, 2051–2067.

Zhu, L. 2001 Simulation of a flapping flexible filament in a flowing soap film by the immersed boundary method. PhD thesis, Courant Institute of Mathematical Sciences, New York University.

Zhu, L. 2007 Viscous flow past an elastic fiber tethered at the middle point: vortex shedding. *J. Fluid Mech.* **587**, 217–234.

Zhu, L. & Peskin, C. S. 2007 Drag of a flexible fiber in a 2D moving viscous fluid. *Computers Fluids* **36**, 398–406.